Formation of Zn-rich phyllosilicate, Zn-layered double hydroxide and hydrozincite in contaminated calcareous soils

Olivier Jacquat[1], Andreas Voegelin[1*], André Villard[2], Matthew A. Marcus[3], Ruben Kretzschmar[1]

[1]Institute of Biogeochemistry and Pollutant Dynamics, Department of Environmental Sciences, ETH Zurich, CHN, CH-8092 Zurich, Switzerland.

[2]Institute of Geology, University of Neuchâtel, CH-2009 Neuchâtel, Switzerland.

[3]Advanced Light Source, Lawrence Berkeley National Laboratory, Berkeley CA 94720, USA.

[*]corresponding author, e-mail: voegelin@env.ethz.ch, phone +41 44 633 61 47, fax ++41 44 633 11 18

Abstract

Recent studies demonstrated that Zn-phyllosilicate- and Zn-layered double hydroxide-type (Zn-LDH) precipitates may form in contaminated soils. However, the influence of soil properties and Zn content on the quantity and type of precipitate forming has not been studied in detail so far. In this work, we determined the speciation of Zn in six carbonate-rich surface soils (pH 6.2 to 7.5) contaminated by aqueous Zn in the runoff from galvanized power line towers (1322 to 30090 mg/kg Zn). Based on 12 bulk and 23 micro-focused extended X-ray absorption fine structure (EXAFS) spectra, the number, type and proportion of Zn species were derived using principal component analysis, target testing, and linear combination fitting. Nearly pure Zn-rich phyllosilicate and Zn-LDH were identified at different locations within a single soil horizon, suggesting that the local availabilities of Al and Si controlled the type of precipitate forming. Hydrozincite was identified on the surfaces of limestone particles that were not in direct contact with the soil clay matrix. With increasing Zn loading of the soils, the percentage of precipitated Zn increased from ~20% to ~80%, while the precipitate type shifted from Zn-phyllosilicate and/or Zn-LDH at the lowest studied soil Zn contents over predominantly Zn-LDH at intermediate loadings to hydrozincite in extremely contaminated soils. These trends were in agreement with the solubility of Zn in equilibrium with these phases. Sequential extractions showed that large fractions of soil Zn (~30% to ~80%) as well as of synthetic Zn-kerolite, Zn-LDH, and hydrozincite spiked into uncontaminated soil were readily extracted by 1 M NH_4NO_3 followed by 1 M NH_4-acetate at pH 6.0. Even though the formation of Zn precipitates allows for the retention of Zn in excess to the adsorption capacity of calcareous soils, the long-term immobilization potential of these precipitates is limited.

1   Introduction

Anthropogenic emissions from industrial activities, traffic, and agriculture lead to the accumulation of heavy metals in soils worldwide. Among the heavy metals, zinc is one of the most extensively used. High Zn concentrations in soils may inhibit microbial activity and cause phytotoxicity. This may lead to reduced soil fertility and crop yields and, in severe cases, to soil degradation and erosion (Alloway, 1995). The bioavailability and mobility of Zn in soils are controlled by its chemical speciation, i.e., by adsorption and precipitation reactions. In acidic soils, Zn predominantly adsorbs by cation exchange. With increasing soil pH, specific Zn adsorption to soil organic matter, clay minerals, oxides and carbonates becomes more relevant. In addition, Zn may also precipitate in high pH soils (Alloway, 1995; Adriano, 2001). Based on thermodynamic data, Zn hydroxide ($Zn(OH)_2$), smithsonite ($ZnCO_3$) or hydrozincite ($Zn_5(OH)_6(CO_3)_2$) have been postulated to control Zn solubility in contaminated neutral and calcareous soils (Schindler et al., 1969; Sharpless et al., 1969; Saeed and Fox, 1977). Spectroscopic work indicated that Zn may also substitute for Ca in the calcite structure (Reeder et al., 1999). To date, however, the formation of hydrozincite, smithsonite or Zn-substituted calcite in contaminated calcareous soils has not been unequivocally confirmed (Manceau et al., 2000; Isaure et al., 2005; Panfili et al., 2005; Kirpichtchikova et al., 2006).

On the other hand, numerous extended X-ray absorption fine structure (EXAFS) spectroscopy studies have shown that the formation of Zn-phyllosilicate or Zn-layered double hydroxide (Zn-LDH) may be quantitatively relevant in slightly acidic to neutral soils contaminated by mining and smelting emissions (Manceau et al., 2000; Juillot et al., 2003; Nachtegaal et al., 2005; Voegelin et al., 2005; Schuwirth et al., 2007). Similar results

were also reported for contaminated calcareous soils (Manceau et al., 2000; Juillot et al., 2003; Isaure et al., 2005; Panfili et al., 2005; Kirpichtchikova et al., 2006). Spectroscopic studies on pristine and contaminated acidic soils demonstrated the incorporation of Zn into the gibbsitic sheets of Al-hydroxy interlayered clay minerals (Zn-HIM) (Scheinost et al., 2002; Manceau et al., 2004; Manceau et al., 2005) and the phyllomanganate lithiophorite (Manceau et al., 2003; Manceau et al., 2004; Manceau et al., 2005). All these recently identified Zn species are layered minerals containing Zn in octahedral sheets.

The formation of layered Zn-bearing precipitates has been documented for soils with variable composition and different source of Zn input. For the assessment of the behavior of Zn in the soil environment, however, more detailed quantitative knowledge about the occurrence and behavior of these Zn species is needed. Firstly, it is essential to understand how soil properties and soil Zn content affect the types and amounts of precipitates forming in a given soil. Secondly, it needs to be established how differences in Zn speciation affect Zn mobility and bioavailability in soil. In order to reliably determine these relations, observations on a larger number of soils are needed. Spectroscopic studies so far considered soils contaminated by mining, smelting or foundry emissions (Manceau et al., 2000; Scheinost et al., 2002; Juillot et al., 2003; Nachtegaal et al., 2005; Voegelin et al., 2005; Schuwirth et al., 2007), deposition of dredged sediments (Isaure et al., 2002; Isaure et al., 2005; Panfili et al., 2005), or sewage irrigation (Kirpichtchikova et al., 2006). In these soils, introduced and soil-formed Zn species could be successfully identified by spatially resolved microfocused (μ-) EXAFS spectroscopy. For the determination of the quantitative abundance of soil-formed Zn-bearing precipitates, on the other hand, bulk EXAFS data need to be analyzed following a linear combination fit (LCF) approach (Manceau et al., 2000). In the presence of substantial fractions of introduced Zn species, especially in the

case of species with a pronounced EXAFS from high-Z backscatterers such as many primary Zn-bearing minerals, however, the EXAFS of whole soil samples may be dominated by introduced Zn species, and the sensitivity and accuracy of LCF analysis regarding the distinction and quantification of different soil-formed Zn species may be limited (Manceau et al., 2000).

In this work, we investigated the speciation and lability of Zn in six calcareous soils, which had been contaminated over several decades with Zn in the runoff water of galvanized power line towers. As these runoff waters contain aqueous Zn^{2+} (Bertling et al., 2006), the distinction and quantification of different soil-formed Zn species can be more reliably achieved than in soils polluted with Zn-bearing contaminants. Focusing on calcareous soils spanning a relatively narrow range in soil pH, we were able to address the effect of Zn loading on Zn speciation in more detail. To determine the speciation of soil Zn, we used bulk- and μ-EXAFS spectroscopy. The fractionation of Zn was determined by single and sequential extractions.

2 Materials and Methods

[Please print Materials and Methods section in small type.]

2.1 *Soil sampling and bulk soil properties*

The soil sampling sites were located in Switzerland between 390 and 1900 m above sea level and varied in exposition and local climatic conditions. Five soils (GLO, TAL, BAS, LAUS, SIS) had developed from limestone (Jura mountain range) and one (LUC2) from dolomite (Swiss Alps). The soils had been contaminated by runoff water from 30 to 55 years old galvanized power line towers. Corrosion of the Zn coating led to soil

contamination with aqueous Zn. About 1 kg of topsoil (0-5 cm) was collected close to the foundation of each tower, where contamination was expected to be highest. The soils were air-dried at room temperature, manually broken into small aggregates, homogenized in an agate mortar, sieved to <2 mm aggregate size and stored in plastic containers at room temperature in the dark. Powdered subsamples <50 μm were prepared by grinding the soil material <2 mm using an agate mill.

The soil pH was determined with a glass electrode in 10 mM $CaCl_2$ (solution-to-soil ratio 10 mL/g). Before analysis, the suspension was shaken for 10 minutes and equilibrated for at least 30 minutes. Total metal contents were quantified by analyzing pressed pellets (4 g soil and 0.9 g Licowax C®) with energy dispersive X-ray fluorescence (XRF) spectrometry (Spectro X-lab 2000). Total carbon (TC) was measured on powdered soil samples using a CHNS analyzer (CHNS-32, LECO). Total inorganic carbon (TIC) was determined by reacting 0.3-0.9 g of soil with 1 M sulfuric acid (H_2SO_4) under heating. The evolving CO_2 was trapped on NaOH-coated support and was quantified gravimetrically. Total organic carbon (TOC) was calculated by subtracting the TIC from the TC content. After the removal of soil organic matter with H_2O_2, the sand content (50-2000 μm) was quantified by wet sieving, the clay content (< 2 µm) by the pipette method (Gee and Or, 2002), and the silt content was calculated. The effective cation exchange capacity (ECEC) was determined by extracting 7 g of soil with 210 mL of 0.1 M $BaCl_2$ for 2 h (Hendershot and Duquette, 1986). After centrifugation, solutions were filtered (0.2 µm, nylon), acidified with 1% (v/v) 30% HNO_3, and analyzed by inductively coupled plasma – optical emission spectrometry (ICP-OES, Varian Vista-MPX). The ECEC was calculated from the extracted amounts of Ca, Mg, K, Na, Al and Mn.

From the soil material >2 mm of SIS, LAUS and BAS, white (WP) and reddish-brown limestone particles (RP) were manually separated. These particles were covered by crusts visible in the light microscope. These crusts were manually isolated for analysis (SIS-WPC, SIS-RPC, LAUS-WPC, and LAUS-RPC; WPC = white particle crust, RPC = reddish-brown particle crust). Even though white limestone particles from BAS were not covered with distinct crusts, surface material was also isolated for analysis (BAS-WPC). From the soils LUC2, GLO, and TAL, white limestone particles were isolated from the soil material <2 mm (LUC2-WP, GLO-WP, and TAL-WP). All samples were ball-milled to <50 μm for analysis by XRF, X-ray diffraction (XRD) and/or EXAFS spectroscopy. XRD patterns were recorded on a Bruker D4 diffractometer (Cu anode, energy dispersive solid state detector; continuous scans from 10° to 40° 2θ with variable slits, 0.02° steps; 18 s/step).

2.2 *Sequential extraction of soils and reference compounds*

The fractionation of Zn in the soils was determined using the 7-step sequential extraction procedure (SEP) of Zeien and Brümmer (1989). Experimental details are provided in Voegelin et al. (2008). Briefly, the extraction consisted of the following steps yielding fractions F1 to F7 (solution-to-soil ratio (SSR) in mL/g; reaction time; hypothetical interpretation according to Zeien and Brümmer (1989)): F1: 1 M NH_4NO_3 (SSR = 25; 24 h; readily soluble and exchangeable); F2: 1 M NH_4-acetate, pH 6.0 (SSR=25; 24 h; specifically adsorbed, $CaCO_3$ bound, and other weakly bound species); F3: 0.1 M NH_2OH-HCl plus 1 M NH_4-acetate, pH 6.0 (SSR=25; 30 min; bound to Mn-oxides); F4: 0.025 M NH_4EDTA, pH 4.6 (SSR=25; 90 min; bound to organic substances); F5: 0.2 M NH_4-oxalate, pH 3.25, in dark (SSR=25; 2h; bound to amorphous and poorly crystalline Fe

oxides); F6: 0.1 M ascorbic acid in 0.2 M NH_4-oxalate, pH 3.25, in boiling water (SSR=25; 2 h; bound to crystalline Fe oxides); F7: XRF analysis (residual fraction). All soils were extracted in duplicates and extracts were analyzed twice using ICP-OES (Varian Vista-MPX).

The sequential extraction was also performed with an uncontaminated non-calcareous topsoil (pH-value 6.5, 15 g/kg TIC., 150 g/kg clay, (Voegelin et al., 2005)) and with quartz powder (Fluka®, Nr. 83340) spiked to 2000 mg/kg Zn using synthetic Zn phases (hydrozincite, Zn-LDH, Zn-kerolite – see next paragraph for details on these minerals). Prior to extraction, the Zn-phases were mixed for 24 h with the dry soil or quartz powder using an overhead shaker.

2.3   *Reference samples for EXAFS spectroscopy*

A series of kerolite-type phyllosilicates containing Zn and Mg in their octahedral sheets were synthesized as described by Decarreau (1980). Briefly, 100 mL of 0.3 M ($ZnCl_2$ + $MgCl_2$) at Zn/(Zn+Mg) ratios of 1, 0.75, 0.5, 0.25, and 0.03 and 20 mL of 1 M HCl were added to 400 mL of 0.1 M $Na_2SiO_4.5H_2O$ under vigorous stirring. The resulting gels were washed and centrifuged three times, before dispersion in 500 mL doubly deionized water (DDI water, 18.2 MΩ·cm, Milli-Q® Element, Millipore). The suspensions were aged for two weeks at 75 °C. Subsequently, they were centrifuged and washed (DDI water) five times, frozen in liquid N_2 (LN) and freeze-dried. XRF analysis indicated Zn/(Zn+Mg) ratios of 1, 0.8, 0.6, 0.34, and 0.06 for the products ("Zn-kerolite", "$Zn_{0.8}Mg_{0.2}$-kerolite", "$Zn_{0.6}Mg_{0.4}$-kerolite", "$Zn_{0.34}Mg_{0.66}$-kerolite", and "$Zn_{0.06}Mg_{0.94}$-kerolite", respectively), i.e, preferential incorporation of Zn over Mg into the precipitate structure. A layered double hydroxide containing Zn and Al in a ratio of 2:1 ("Zn-LDH")

8

was synthesized according to Taylor (1984). Hydroxy-Al interlayered montmorillonite (HIM) was prepared by slowly titrating a suspension of 20 g/L montmorillonite (SWy-2, Clay Mineral Society) and 40 mmol/L $AlCl_3$ to pH 4.5 (Lothenbach et al., 1997). After equilibration for 15 h, the precipitate was washed four times, frozen in LN and freeze-dried. Zn in HIM ("Zn-HIM", 6900 mg/kg Zn) was obtained by suspending 1 g of HIM in a 500 mL 2 mM $ZnCl_2$ plus 10 mM $CaCl_2$ solution for 15 h at pH 5.0. The product was washed, frozen using LN and freeze-dried. Natural Zn-containing lithiophorite ("Zn-lithiophorite") from Cornwall, Great Britain, was kindly provided by Beda Hofmann (Natural History Museum Berne, Switzerland).

Amorphous $Zn(OH)_2$ ("$Zn(OH)_2$") was prepared by adding 66 ml 25% NH_3 to 500 mL 1 M $Zn(NO_3)_2$ (Genin et al., 1991). The solution was vigorously stirred and purged with N_2. After 2 h, the precipitate was centrifuged and washed five times in DDI water, frozen in LN and freeze-dried. For the synthesis of Zn-substituted calcite ("Zn-calcite"), vaterite was first produced by adding 500 mL 0.4 M $CaCl_2$ to 500 mL 0.4 M Na_2CO_3, using N_2-saturated DDI water (Schosseler et al., 1999). The vaterite was obtained by filtration of the suspension. Four g of wet vaterite were reacted with 200 mL of 460 μM $ZnCl_2$ during 5 d at room temperature, resulting in Zn-substituted calcite of composition $Zn_{0.003}Ca_{0.997}CO_3$ ("Zn-calcite"). The precipitate was washed, frozen and freeze-dried. $Zn_5(OH)_6(CO_3)_2$ ("hydrozincite", Alfa Aesar, Nr. 33398) and $Zn_3(PO_4)_2$ (anhydrous "Zn-phosphate", Alfa Aesar, Nr. 13013) were used without further treatment. Natural $ZnCO_3$ ("smithsonite") from Namibia was kindly provided by André Puschnig (Natural History Museum Basel, Switzerland).

For the preparation of birnessite with high and low Zn content, Na-buserite was first synthesized by mixing cooled (<5°C) 200 mL 0.5 M $Mn(NO_3)_2$ into 250 mL DDI water

containing 55 g NaOH under vigorous stirring (Giovanoli et al., 1970; Feng et al., 2004). After oxidation for 5 h with bubbling O_2, the precipitate was separated by centrifugation, washed with DDI water until the pH was close to 9, and stored wet. Eight g of wet Na-buserite were dispersed in 1 L Ar-saturated 0.1 M $NaNO_3$ in the dark. Sorption of Zn at Zn/Mn ratios of 0.088 ("high Zn birnessite") and 0.003 ("low Zn birnessite") was achieved by adding appropriate amounts of $Zn(NO_3)_2$ keeping the suspension at pH 4 using a pH-stat apparatus (Titrando, Metrohm®) (Lanson et al., 2002). After equilibration for 3 h, the samples were filtered, frozen using LN and freeze-dried. Zn complexed by phytate ("Zn-phytate") was prepared by adding 1.2 mmol $Zn(NO_3)_2$ and 200 μL of triethylamine to a mixed solution of 20 mL DDI water and 20 mL methanol containing 0.27 mmol of inositol hexaphosphoric acid (Rodrigues-Filho et al., 2005). The solution was stirred for 3 h at 60°C. The product was then filtered, frozen and freeze-dried. Zn was adsorbed to ferrihydrite ("Zn sorbed Fh") by reacting 0.8 g of freeze-dried ferrihydrite with 800 mL mM $Zn(NO_3)_2$ and 100 mM $NaNO_3$ at pH 6.5 during 24 h (Waychunas et al., 2002), resulting in a Zn content of 28600 mg/kg Zn. The sample was then separated by centrifugation, frozen in LN and freeze dried. Aqueous Zn ("aq. Zn") was analyzed as a 0.5 M $ZnNO_3$ solution. An EXAFS spectrum of Zn adsorbed to calcite ("Zn sorbed Cc", 1200 mg/kg Zn) was kindly provided by Evert Elzinga (Rutgers University). The sample had been prepared by spiking a solution of 0.45 g/L calcite with 10 μM $ZnCl_2$ (Elzinga and Reeder, 2002).

The structure of synthetic Zn-bearing precipitates (ZnMg-kerolites, Zn-LDH, Zn-HIM, Zn-calcite, amorphous $Zn(OH)_2$), Zn sorbent phases (birnessite, ferrihydrite), natural specimens (lithiophorite, smithsonite), and purchased chemicals (hydrozincite, Zn-phosphate) was confirmed by X-ray diffraction analysis.

10

2.4 Acquisition of bulk Zn K-edge EXAFS spectra

Bulk Zn K-edge (9659 eV) EXAFS spectra at room temperature were collected at the beamline X11A at the National Synchrotron Light Source (NSLS, Brookhaven, USA) and at the XAS beamline at the Angströmquelle Karlsruhe (ANKA, Karlsruhe, Germany). Powdered soil samples and reference materials were mixed with polyethylene or Licowax C® and pressed into 13-mm pellets for analysis in fluorescence or transmission mode. The energy was calibrated using a metallic Zn foil (first maximum of the first derivative of the adsorption edge at 9659 eV). At NSLS, the Si(111) monochromator was manually detuned to 75 % of maximum intensity. Fluorescence spectra were recorded using a Stern-Heald-type detector filled with Ar gas and a Cu filter (edge jump $\Delta\mu t=3$) to reduce the intensity of scattered radiation. At ANKA, the Si(111) monochromator was detuned to 65% using a software-controlled monochromator stabilization. Fluorescence spectra were collected with a 5-element Ge solid state detector. Zn-lithiophorite was analyzed at the Dutch Belgian Beamline (DUBBLE) at the European Synchrotron Radiation Facility (Grenoble, France) using a similar setup as at the XAS beamline (ANKA).

2.5 μ-XRF and μ-EXAFS analyzes on soil thin sections

Freeze-dried soil aggregates of soils GLO, SIS and LUC2 were embedded in high purity resin (Epofix Struers or Araldit 2020). Polished thin sections (30-45 μm thick) were prepared on glass slides. From LUC2, also a free standing section (30 μm thick) was prepared. The thin sections were analyzed at the beamline 10.3.2 at the Advanced Light Source (ALS, Berkeley, USA) (Marcus et al., 2004). The sections were mounted at 45° to the incident beam and the fluorescence signal was recorded at 90° using a 7-element Ge solid state detector. Element distribution maps were obtained at incident photon energies of

10 keV and 7.012 keV (100 eV below Fe K-edge) with resolutions (step sizes) of 20×20 or 5×5 μm^2 and dwell times of 100, 150 or 200 ms/point. At selected points of interest (POI), fluorescence spectra (10 keV) and Zn K-edge EXAFS spectra were recorded using a beam size between 5×5 and 16×7 μm^2, depending on local Zn concentration and the size of the feature of interest.

2.6   *EXAFS spectra extraction and analysis by PCA, TT, and LCF*

EXAFS spectra were extracted using the software code Athena (Newville, 2001; Ravel and Newville, 2005). The first maximum of the first derivative of the absorption edge was used to set E_0. Normalized absorption spectra were obtained by subtracting a first order polynomial fitted to the pre-edge data (-150 to -30 eV relative to E_0) and subsequently dividing through a second order polynomial fitted to the post-edge data (+150 eV up to 100 eV before end of spectrum). EXAFS spectra were extracted by fitting the post-edge data (0.5 to 12 $Å^{-1}$) with a cubic spline function and minimizing the amplitude of the Fourier transform at radial distances <0.9 Å (Autobk algorithm, k-weight = 3; R_{bkg} = 0.9 Å).

Principal component analysis (PCA) and target transform testing (TT) were carried out using Sixpack (Webb, 2005). All k^3-weighted bulk- and micro-EXAFS spectra were analyzed over the k-range 2 to 10 $Å^{-1}$. The number of components required to reproduce the entire set of spectra without experimental noise was determined by PCA based on the empirical indicator function (IND) (Malinowski, 1977). TT based on the significant components was then used to determine the suitability of reference spectra to describe the experimental data. This assessment was based on the empirical SPOIL value (Malinowski, 1978) and the normalized sum of squared residual (NSSR) of the target transforms (Isaure et al., 2002; Sarret et al., 2004; Panfili et al., 2005; Kirpichtchikova et al., 2006).

Using the selected reference spectra, the experimental spectra were analyzed by linear combination fitting (LCF) using the approach and software developed by Manceau et al. (1996; 2000). The LCF analysis was carried out by calculating all possible 1-component to 4-component fits based on all reference spectra selected from PCA and TT. Starting from the best 1-component fit as judged by the lowest NSSR (NSSR = $(\Sigma_i(k^3\chi_{exp}-k^3\chi_{fit})^2)/\Sigma_i(k^3\chi_{exp}^2)$, additional references were considered in the fit as long as they resulted in a decrease in NSSR by at least 10 %. The overall precision of LCF with respect to fitted fractions of individual reference spectra has previously been estimated to 10% of the total Zn (Isaure et al., 2002). However, the detection limit, precision, and accuracy of LCF analyses depend on the EXAFS of individual species of interest, structural and spectral similarities between different phases in mixtures, and the availability of a database including all relevant reference spectra (Manceau et al., 2000).

2.7   *Calculation of Zn solubility in equilibrium with Zn-containing precipitates*

The solubility of Zn was calculated in equilibrium with different Zn-bearing phases (composition; ion activity product (IAP); log solubility product ($logK_{so}$)): Amorphous Zn hydroxide ($Zn(OH)_2$; $(Zn^{2+})(H_2O)^2(H^+)^{-2}$; 12.47), zincite ($ZnO$; $(Zn^{2+})(H_2O)^2(H^+)^{-2}$; 11.19), smithsonite ($ZnCO_3$; $(Zn^{2+})(CO_3^{2-})$; -10.0), hydrozincite ($Zn_5(CO_3)_2(OH)_6$; $(Zn^{2+})^5(CO_3^{2-})^2(H_2O)^6(H^+)^{-6}$; 8.7, (Preis and Gamsjager, 2001)), Zn-LDH ($Zn_2Al(OH)_6(CO_3)_{0.5}$; $(Zn^{2+})^2(Al^{3+})(H_2O)^6(CO_3^{2-})^{0.5}(H^+)^{-6}$; 11.19, (Allada et al., 2006)), Zn-kerolite ($Zn_3Si_4O_{10}(OH)_2$; $(Zn^{2+})^3(H_4SiO_4)^4(H_2O)^{-4}(H+)^{-6}$; 6.7, calculated from predicted $\Delta G^0_{f,298K}$ (Vieillard, 2002)), Zn-chlorite ($(Zn_5Al)(Si_3Al)O_{10}(OH)_8$; $(Zn^{2+})^5(Al^{3+})^2(H_4SiO_4)^3(H_2O)^6(H+)^{-16}$; 37.6, calculated from predicted $\Delta G^0_{f,298K}$ (Vieillard, 2002)). Activity corrections and complexation of aqueous Zn were not included. Zn

solubility was calculated for atmospheric (pCO_2 = 3.2×10^{-4} atm, "low CO_2") and hundredfold atmospheric CO_2 partial pressure ("high CO_2"). "Low Al" and "high Al" scenarios were calculated for Al^{3+} in equilibrium with gibbsite and amorphous Al-hydroxide, respectively ($Al(OH)_3$; $(Al^{3+})(H_2O)^3$ $(H^+)^{-3}$; 8.11 and 10.8). For "low Si" and "high Si" calculations, silicic acid was assumed to be in equilibrium with quartz and amorphous silica, respectively (SiO_2; $(H_4SiO_4)(H_2O)^{-2}$; -2.74 and -4.0). Unless otherwise stated, equilibrium constants were taken from the MinteqA2 V4 database (Allison et al., 1991).

3 Results

3.1 Bulk soil characteristics

Selected properties of the soil samples are reported in Table 1. The 6 soils had pH values between 6.2 and 7.5 and covered a wide range in TIC (1 to 89 g/kg), clay content (90 to 450 g/kg), and ECEC (99 to 410 $mmol_c$/kg). Contamination with aqueous Zn from corroding power line towers over 30 to 55 years had led to the accumulation of 1322 to 30090 mg/kg Zn in the topsoil layers. In Switzerland, 150 mg/kg Zn represents an upper level for typical geogenic Zn contents and soils with more than 2000 mg/kg Zn are considered to be heavily contaminated (VBBo, 1998). In Table 1, the soils are arranged by increasing total Zn content divided by clay content (Zn/Clay).

3.2 Principal component analysis and target transform testing

Before considering the speciation of Zn in individual soils, we performed a principal component analysis (PCA) with all 35 EXAFS spectra (bulk soils (6), limestone crusts/particles (6), μ-EXAFS spectra from GLO (5), LUC2 (9), and SIS (9)) to determine

14

the number of distinguishable spectral components. The parameters of the first 8 components obtained by PCA are given in Table 2. The IND function reached a minimum for 5 spectral components. The first 5 components explained 70% of the total experimental variance and provided a good reconstruction of all 35 EXAFS spectra (NSSR 0.5 to 6.8 %).

We therefore used the first 5 components from PCA for the assessment of reference spectra by target transform testing (TT) (Table 3), considering references with SPOIL values below 6 in subsequent LCF analysis of experimental data (see footnote of Table 3 for classification of SPOIL values). Among all tested references, aqueous Zn had the lowest SPOIL value. TT also returned a low SPOIL for hydrozincite, Zn-rich kerolites, and $Zn(OH)_2$, while the SPOIL of Zn-LDH was slightly higher. Also Zn sorbed ferrihydrite and calcite and Zn-phytate were classified as good references based on their SPOIL values. The SPOIL of Zn in kerolite phases increased with decreasing Zn/(Zn+Mg) ratio, paralleled by an increase in the NSSR of the respective target transform. SPOIL values of low Zn-birnessite, smithsonite, Zn-calcite, and high Zn-birnessite classified these references as good to fair. However, the high NSSR of their target transform, i.e., the deviation between the experimental and the reconstructed spectra shown in Fig. 1, suggested that these Zn species were dominant in the samples. The high SPOIL (>6) and NSSR of Zn-HIM and Zn-lithiophorite containing Zn in octahedral sheets surrounded exclusively by light Al atoms indicated that this type of coordination environment was not relevant in the studied soils. These two latter references were therefore not considered for LCF. Overall, PCA combined with TT indicated that reference spectra of ZnMg-kerolite, Zn-LDH, hydrozincite, smithsonite, $Zn(OH)_2$ and adsorbed/complexed Zn species in octahedral and tetrahedral coordination (aqueous Zn, Zn-phytate, Zn sorbed calcite, Zn sorbed ferrihydrite, Zn-phosphate, low- and high Zn-birnessite) were suitable to describe the experimental EXAFS

spectra by LCF. A more detailed structural characterization of selected reference spectra based on shell fitting is provided in the electronic annex.

The number of suitable reference spectra identified by TT was higher than the number of principal components from PCA. This may be related to the occurrence of species uniformly distributed throughout the samples (Manceau et al., 2002) or to spectral similarities between different reference spectra (Sarret et al., 2004). Furthermore, the principal components identified by PCA may also reflect the dominant backscattering signals occurring in variable proportions in different Zn species. In Zn-LDH and all Zn-kerolite phases, octahedrally coordinated Zn is contained in octahedral sheets surrounded by variable amounts of Zn and Mg/Al/Si in the second shell (Zn/Mg/Al in octahedral sheet, Si in adjacent tetrahedral sheet, see electronic annex for further details). In Zn-phosphate, Zn sorbed calcite, Zn sorbed ferrihydrite, and Zn-phytate, on the other hand, Zn is tetrahedrally coordinated. The EXAFS spectra of tetrahedral Zn in sorbed or complexed form are dominated by the first-shell Zn-O signal and are therefore relatively similar (Fig. 1). This complicated the distinction of these species in experimental spectra with several spectral contributions. In LCF, we therefore quantified tetrahedrally coordinated sorbed Zn ("sorbed [IV]Zn") without differentiating using the reference providing the lowest NSSR. Similarly, the spectrum of aqueous Zn was used as the only proxy for octahedrally coordinated Zn bound as an outer-sphere sorption complex or as an inner-sphere complex with weak backscattering from atoms in the sorbent phase.

3.3   *Microscale speciation of Zn in soil GLO*

Light microscope images from a thin-section of soil GLO together with Zn, Ca, Fe, and Mn distribution maps are shown in Figure 2. High Zn concentrations occured in FeMn-

nodules present throughout the soil section. At lower concentrations, Zn was also present within the clayey soil matrix. EXAFS spectra collected on selected POI are shown in Figure 3. LCF parameters are provided in Table 4.

Two μ-EXAFS spectra (GLO-4 and GLO-5) were recorded within a large FeMn-nodule shown in more detail in Figure 2C. Higher Zn concentrations were observed in Mn-rich than in Fe-rich zones of the nodule. The spectrum of the Mn-rich interior of the nodule (GLO-5) exhibited a splitting of the second EXAFS oscillation near 6 $Å^{-1}$ (Fig. 3). This splitting, though more pronounced, is typical for Zn adsorbed to birnessite at low surface coverage (Fig. 1). The relative height of the Kα fluorescence lines of Mn, Fe, and Zn (Mn/Fe/Zn ≈ 1.4/1/1) suggested that Zn may be associated with both Mn- and Fe-(hydr)oxides. Based on these observations, the LCF of GLO-5 (Table 4, Fig. 3) was based on low Zn-birnessite and Zn sorbed ferrihydrite (NSSR 12.1%), even though a better fit (NSSR 7.1%,) would have been obtained with 42% low Zn-birnessite and 64% Zn-phytate. Zn-birnessite has previously been identified in a marine FeMn-nodule (Marcus et al., 2004) as well as in natural (Manceau et al., 2003; Isaure et al., 2005) and contaminated soils (Manceau et al., 2000; Isaure et al., 2005; Voegelin et al., 2005). The spectrum from the Fe-rich zone of the nodule (GLO-4) did not exhibit the splitting at ~6 $Å^{-1}$ observed for GLO-5 and was best described by a 1-component fit using the spectrum of Zn sorbed ferrihydrite (Table 4). This suggested that Fe-(hydr)oxides were likely the main sorbent for Zn, in line with the relative heights of the Kα fluorescence lines (Mn/Fe/Zn ≈ 2/10/1) indicating a much higher Fe/Mn ratio than in the Mn-rich zone of the nodule. The spectrum GLO-2 closely resembled the Zn-phytate reference (Figs. 1 and 3, Table 4), suggesting that Zn at this location was mainly tetrahedrally coordinated and complexed by organic phosphate

groups (Sarret et al., 2004). The spectrum GLO-1 exhibited the spectral features of Zn-LDH (Fig. 1 and 3), as reflected by the results from LCF (Table 4).

3.4   *Microscale speciation of Zn in soil LUC2*

The distribution of Ca in the soil thin section of soil LUC2 reflected the high content of mostly dolomite sand (781 g/kg) in this soil (Fig. 4). The Zn distribution indicated localized Zn rich zones and Zn at lower concentrations associated with organic material. Except for a prominent FeMn-nodule, the distribution of Zn was not closely related with Fe and Mn. While the POI LUC2-1 to LUC2-7 were located on the thin section shown in Fig. 4, LUC2-8 and LUC2-9 were analyzed on a second thin section. The EXAFS spectra for LUC2-1 to LUC2-9 together with LCF spectra are shown in Fig. 5. LCF parameters are listed in Table 5.

The EXAFS spectrum collected on an organic fragment (LUC2-1) closely matched the Zn-phytate reference (Figs. 1 and 4), indicating the presence of organically complexed tetrahedral Zn (Sarret et al., 2004). In contrast, LCF of the spectra LUC2-2 and LUC2-7 located next to dolomite grains returned substantial fractions of Zn sorbed calcite as best proxy for tetrahedrally coordinated sorbed Zn. The spectrum LUC2-4 collected on a Zn-rich spot of ~25 µm diameter perfectly matched the reference spectrum of $Zn_{0.8}Mg_{0.2}$-kerolite (Fig. 5, Table 5). The spectrum LUC2-8 collected on another Zn-rich spot, however, revealed the typical features of Zn-LDH (Fig. 5). The best LCF was achieved with a mixture of 103% Zn-LDH and 18% $Zn_{0.8}Mg_{0.2}$-kerolite (Table 5). The deviation of the sum of fitted fractions from 100 % may be related to slight differences in the mineral structure and crystallinity of the sample and reference material (Manceau et al., 2000). Inspection of the Fourier-transformed EXAFS spectra LUC2-4 and LUC2-8 and their LCF

(Fig. EA2, electronic annex) further confirmed that the spectrum LUC2-4 was nearly identical to the spectrum of $Zn_{0.8}Mg_{0.2}$-kerolite and that the spectrum LUC2-8 was best described by Zn-LDH and a minor fraction of $Zn_{0.8}Mg_{0.2}$-kerolite. In addition to Zn-kerolite (spectrum LUC2-4) and Zn-LDH (spectrum LUC2-8), the LCF of the spectra LUC2-6 and LUC2-7 further suggested that also hydrozincite may locally form within the same soil environment.

3.5   *Microscale speciation of Zn in soil SIS*

Distribution maps of Zn, Ca, and Fe in a thin section from soil SIS are shown in Figure 6. The maps indicated the presence of limestone particles embedded in a clayey soil matrix rich in Zn and Fe. As in the soils LUC2 and GLO, Mn was present in discrete FeMn-nodules. The entire soil matrix was rich in Zn, reflecting the extremely high Zn content of soil SIS (Table 1). Due to the high Zn contents throughout the soil matrix, no enrichment of Zn was observed in FeMn-nodules.

Micro-EXAFS and corresponding LCF spectra of 9 POI (SIS-1 to SIS-9) are shown in Figure 7. LCF parameters are provided in Table 6. The spectra SIS-1, SIS-2, SIS-3 did not exhibit pronounced high frequency features and LCF returned a high fraction of tetrahedrally coordinated Zn (Zn sorbed to calcite) at these locations. The μ-EXAFS spectra SIS-4 to SIS-9 (except SIS-6) were best fitted with Zn-LDH and minor contributions of Zn-phyllosilicate ($Zn_{0.8}Mg_{0.2}$-kerolite) and sorbed ^{IV}Zn. None of the analyzed POI indicated the presence of hydrozincite.

3.6   *Speciation of Zn associated with limestone particles*

In addition to the aggregated matrix, all soils also contained isolated white limestone particles. White limestone particles from soils SIS and LAUS were covered with massive up to 0.5 mm thick crusts (light microscope images shown in Fig. EA4, electronic annex). The XRD pattern showed that the crust material from soil SIS consisted mainly of hydrozincite (Fig. EA5, electronic annex). XRD patterns of crusts from soils BAS and LAUS also indicated traces of hydrozincite, but were dominated by calcite and quartz (Fig. EA5). EXAFS analysis (Fig. 8, Table 7) confirmed that hydrozincite was the only Zn-bearing phase in the sample SIS-WPC. No crusts were observed on limestone particles from the soils TAL, GLO, and LUC2, and XRD patterns of powdered limestone samples did not show any diffraction peaks of hydrozincite (not shown). However, EXAFS spectra revealed that a significant fraction of Zn associated with limestone particles from LUC2 and TAL was hydrozincite (Fig. 8, Table 7). For the soil GLO with lowest Zn content, LCF indicated that most Zn on limestone particles was adsorbed to the calcite surface.

Soils SIS and LAUS also contained reddish-brown limestone particles consisting mainly of calcite and quartz. These particles were covered with thin crusts of black, brown and red color (Fig. EA4). XRD patterns of these crusts indicated the presence of clay minerals, quartz, calcite, feldspars and goethite, but hydrozincite was not detected (not shown). EXAFS spectroscopy showed that about two thirds of Zn in these crusts was sorbed [IV]Zn and Zn-rich kerolite, and that only about one third was contained in hydrozincite (Fig. 8, Table 7).

3.7   Speciation of Zn in whole soils by bulk EXAFS spectroscopy

The EXAFS spectra of the bulk soil samples and corresponding LCF spectra are shown in Figure 9. LCF results are provided in Table 8. The sum of the fitted fractions of Zn-rich kerolite ($Zn_{0.8}Mg_{0.2}$-kerolite or $Zn_{0.6}Mg_{0.4}$-kerolite), Zn-LDH, and hydrozincite (Σppt) indicates the total fraction of Zn contained in precipitates, and the sum of sorbed ^{IV}Zn and aqueous Zn (Σsorbed) represents the percentage of adsorbed and complexed Zn in tetrahedral and octahedral coordination. The percentage of precipitated Zn increased with increasing Zn/clay content (total Zn normalized over clay content, Table 1), showing that the speciation of Zn systematically shifted with Zn loading of the soils.

The low percentages of precipitates in soils GLO and LUC2 complicated the differentiation between Zn-LDH and ZnMg-kerolite. Using either Zn-LDH or $Zn_{0.8}Mg_{0.2}$-kerolite as proxy for precipitated Zn resulted in LCF with similar NSSR (see Fig. EA3 and Table EA2 in electronic annex for details). Since only Zn-LDH was detected in the soil thin section of soil GLO, the fit based on Zn-LDH was listed in Table 8. For soil LUC2, the LCF based on $Zn_{0.8}Mg_{0.2}$-kerolite provided a visually better match to the Fourier-transformed EXAFS signal in the region of the second-shell (Fig. EA3). Furthermore, pure $Zn_{0.8}Mg_{0.2}$-kerolite was identified in the soil thin section (Fig. 5 and Table 5). Therefore, the LCF based on $Zn_{0.8}Mg_{0.2}$-kerolite was reported in Table 5. In the higher contaminated soils BAS and LAUS, about half of the total Zn was associated with neoformed precipitates (Table 8). LCF based on Zn-LDH and minor fractions of sorbed ^{IV}Zn and aqueous Zn satisfactorily reproduced the experimental spectra (Fig. EA3). However, adding $Zn_{0.8}Mg_{0.2}$-kerolite to the LCF led to a further decrease in the NSSR (Table EA2) and improved the quality of the fit in the region of the second shell (Fig. EA3, Table EA2), suggesting that a

minor fraction of a ZnMg-kerolite-type precipitate may have formed in addition to Zn-LDH. Only slightly higher NSSR were obtained if Zn-kerolite or $Zn_{0.6}Mg_{0.4}$-kerolite instead of $Zn_{0.8}Mg_{0.2}$-kerolite were used for LCF, due to the similarity in the respective reference spectra. Thus, the LCF of individual spectra was not sensitive to the exact Zn/(Zn+Mg) ratio of Zn-rich phyllosilicates. The similar LCF results for soils BAS and LAUS supported the assumption that comparable soil physicochemical conditions and Zn content result in similar Zn speciation. For the soils TAL and SIS with extreme Zn/clay contents (Table 1), LCF indicated that about half of the total soil Zn was bound in hydrozincite (Table 8). This finding was in agreement with the identification of hydrozincite crusts on limestone particles from both soils (Table 7, Fig. EA5).

3.8   *Sequential extraction of Zn from spiked and contaminated soils*

Sequential extraction results are presented in Figure 10 (absolute amounts of extracted Zn, Fe, and Mn are reported in the electronic annex, Table EA3). The extractability of synthetic references spiked into a neutral non-calcareous soil increased in the order Zn-kerolite, Zn-LDH, hydrozincite. Sequential extractions with spiked quartz powder indicated the same sequence of extractability. Comparison between spiked soil and spiked quartz powder demonstrated that sequential extraction results for spiked soil were greatly affected by readsorption or reprecipitation (Gleyzes et al., 2002). Considering that the fractions F1 and F2 are intended to release mobile and easily mobilizable Zn (Zeien and Brümmer, 1989), respectively, all 3 Zn-species were readily extractable at slightly acidic pH of 6.0 in the presence of a complexing ligand (acetate). Rapid dissolution of Zn-LDH has also been observed at more acidic pH of 3.0 (Voegelin and Kretzschmar, 2005).

The lowest mobilizable percentage of total Zn (29% in F1+F2) was found for soil GLO, which contained the lowest fraction of precipitated Zn (Table 8). In contrast, between 59 and 83% of total Zn in the other soils was extracted in F1+F2, indicating that most Zn was present in labile form. Although hydrozincite represented about half of the total Zn in these soils, sequential extraction results from soil TAL were in much better agreement with the fractionation behaviour of hydrozincite than results from soil SIS. This observation can be related to the higher clay content, organic carbon content, and Zn content of soil SIS; factors favoring readsorption and reprecipitation during sequential extraction (Kheboian and Bauer, 1987; Shan and Bin, 1993).

3.9   *Solubility of Zn in thermodynamic equilibrium with Zn-bearing precipitates*

Solubility calculations for Zn in equilibrium with a series of Zn-bearing mineral phases are shown in Figure 11. Amongst the Zn (hydr)oxides and Zn (hydroxy)carbonates, hydrozincite is the thermodynamically most stable phase at typical soil pCO_2 levels. Formation of Zn (hydr)oxides might only occur at unrealistically low soil pCO_2. At high CO_2 partial pressure, smithsonite and hydrozincite result in similar Zn solubility. However, formation of smithsonite is limited by its slow precipitation kinetics relative to hydrozincite (Schindler et al., 1969). Even if low Si and Al concentrations in equilibrium with quartz and gibbsite are considered, Zn-phyllosilicates and Zn-LDH result in much lower Zn solubilities than hydrozincite, smithsonite, and Zn (hydr)oxides. Higher concentrations of Si and Al in equilibrium with amorphous SiO_2 and $Al(OH)_3$ and high pCO_2 even further decrease the solubility of Zn in equilibrium with Zn-phyllosilicates and Zn-LDH. With respect to Zn-phyllosilicates and Zn-LDH, the calculations indicate that the availabilities of Si and Al and the pCO_2 are critical in the control of the least soluble phase. In previous

studies (Panfili et al., 2005; Voegelin et al., 2005), the solubility of Zn in the presence of Zn-LDH was estimated from a $logK_{so}$ of 19.94. This value had been derived from dissolution equilibria (Johnson and Glasser, 2003). Here, we used a considerably lower $logK_{so}$ of 11.19 determined by calorimetry (Allada et al., 2006). Based on this $logK_{so}$, the solubility of Zn in equilibrium with Zn-LDH varies in a similar range as in equilibrium with Zn-phyllosilicates. Depending on the concentrations of dissolved Al, Si, and CO_2, formation of Zn-LDH may even be thermodynamically favored over the formation of Zn-phyllosilicates, in contrast to trends previously estimated on the basis of the higher $logK_{so}$ from Johnson and Glasser (2003).

4   Discussion

4.1   Changes in speciation with Zn loading and soil properties

Within the studied set of calcareous soils, increasing Zn loading (as indicated by Zn content divided by the clay size mass fraction) resulted in increasing precipitate formation and in a shift in precipitate type. (Tables 1 and 8). These observations can be interpreted as a sequence of increasing Zn input into soil. Initially, Zn uptake is dominated by adsorption mechanisms. Adsorbed/complexed Zn species identified in soil thin sections included tetrahedrally coordinated Zn complexed by organic functional groups, adsorbed to Fe- and Mn-(hydr)oxides, and to calcite as well as octahedrally coordinated adsorbed Zn (outer-sphere or inner-sphere). With increasing saturation of adsorption sites, dissolved Zn concentrations increase and at some point exceed the solubility limits of Zn-bearing precipitates. In the soils GLO and LUC2, which had the lowest Zn contents within the studied set of soils, Zn-LDH and/or Zn-phyllosilicate formed, but represented minor

24

fractions of the total Zn (Table 8). Depletion of readily available Si at higher Zn loadings may explain the predominant formation of LDH-type precipitates in soils BAS and LAUS. Finally, extreme Zn input may deplete the readily available pools of both Si and Al, leading to the formation of hydrozincite. This was observed for the soil SIS and TAL with highest Zn loading relative to their clay contents as well as locally on calcite particles from all soils except GLO. Overall, the observed trends in the extent and type of Zn precipitate formation with increasing Zn loadings can be rationalized based on the availability of adsorption sites, Si and Al. In the present study, no clear relation between precipitate formation and soil pH was found. This can be attributed to the relatively narrow pH-range (pH 6.2 to 7.5) of the investigated carbonate-buffered soils.

4.2   Changes in Zn extractability with Zn loading and soil properties

Increasing Zn loading resulted in increasing precipitate formation and in a shift to precipitates which were found to be more readily released by sequential extraction when spiked into uncontaminated soils. The sequential extraction data from contaminated soils only partly reflected these trends, due to readsorption and reprecipitation phenomena that depend on Zn loading. However, the lower percentage of Zn extracted in F1+F2 from soil GLO than from soils with higher percentages of precipitated Zn clearly demonstrate that the incorporation of Zn into these precipitates does not correspond to a reduction in the extractability of Zn.

In contrast to Zn speciation inferred from EXAFS spectroscopy, which mainly varied with Zn loading, Ba-exchangeable fractions of Zn substantially varied with the availability of adsorption sites (ECEC, organic carbon content, clay content) and with adsorption affinity (controlled by soil pH) (Table 1). Although soil GLO contained ~5

25

times less Zn than soil TAL, its exchangeable Zn content was ~10 times higher. This reflected the much higher ECEC, clay and organic carbon content and the lower pH of soil GLO. Comparison of the soils LUC2 and LAUS, on the other hand, showed that higher Zn content at similar ECEC resulted in a higher exchangeable Zn content.

4.3   *Formation and structure of layered Zn-precipitates*

Previous studies demonstrated the formation of Zn-rich phyllosilicate and Zn-LDH in contaminated soils under field conditions (Juillot et al., 2003; Nachtegaal et al., 2005; Panfili et al., 2005; Voegelin et al., 2005). In the soil LUC2, we identified both types of precipitates in nearly pure form at different locations (Fig. 5, Table 5), likely as a consequence of differences in local chemical conditions.

Regarding the formation of Zn-phyllosilicate, the LCF of bulk- and μ-EXAFS spectra based on the reference spectra of Zn-rich kerolites were consistently better than fits based on the spectrum of pure Zn-kerolite. This observation is in agreement with previous EXAFS studies on the speciation of Zn in contaminated calcareous soils (Manceau et al., 2000; Kirpichtchikova et al., 2006) and suggests that the formation of Zn-rich phyllosilicates is favored over the formation of the pure Zn-phyllosilicate endmember in the soil environment.

For many μ-EXAFS spectra for which LCF indicated the presence of Zn-LDH, the fits were significantly improved by including a minor fraction of Zn-rich kerolite (on average 14% of the sum of Zn-LDH and Zn-kerolite considering all μ-EXAFS for which LCF indicated Zn-LDH (n=14), Tables 4, 5 and 6). Similarly, Zn-kerolite accounted for about 25% of the precipitate fraction (Zn-LDH + Zn-kerolite) in the EXAFS spectra of BAS and LAUS (Table 8). The same Zn-LDH over Zn-kerolite ratio was obtained in a

26

previous study on the speciation of Zn in a soil contaminated by ZnO (Voegelin et al., 2005). There are at least five possible processes which could explain these observations: 1) The formation of mainly Zn-LDH and a minor fraction of Zn-phyllosilicate is related to the kinetics of precipitate formation and the supply of Si and Al (Voegelin et al., 2005). 2) Rapid formation of Zn-LDH is followed by silicate incorporation into the interlayer and transformation of Zn-LDH into Zn-phyllosilicate (Depège et al., 1996; Ford and Sparks, 2000). 3) Formation of Zn-phyllosilicate is followed by Zn-LDH formation after depletion of readily available Si. 4) Precipitates with phyllosilicate- and LDH-type structural features are forming. 5) A substantial fraction of total Zn is adsorbed at the edges of clay minerals.

Concerning the second possibility, experimental evidence for the transformation of Zn-LDH into Zn-phyllosilicate is still lacking. However, hexagonal zaccagnaite crystals (Zn-LDH mineral) in calcite veins in marble were found to be covered with a thin crust of fraipontite (Zn-phyllosilicate) (Merlino and Orlandi, 2001), which may have formed from zaccagnaite in contact with Si-rich water. On the other hand, Zn speciation in a non-calcarous soil (pH 6.5, 15 g/kg org. C, 150 g/kg clay, 2800 mg/kg Zn) stabilized within 9 months after contamination with ZnO and about half of the Zn was incorporated into precipitates which were fit by ~75% Zn-LDH and ~25% Zn-phyllosilicate (Voegelin et al., 2005). Almost the same Zn speciation was found for soils BAS and LAUS with similar soil characteristics after 3 decades of soil contamination. This suggests that transformation of Zn-LDH into Zn-phyllosilicate has not occurred to a major extent within this period of time. Regarding the third possibility - initial Zn-phyllosilicate formation followed by Zn-LDH precipitation at increasing Zn loading - it is worth noting that this interpretation is in line with the trend in precipitate type observed in our bulk soils. Concerning the fourth possibility, examples for layered Zn-species with structural features of both Zn-kerolite and

Zn-LDH include Zn-chlorite ((Zn_5Al)(Si_3Al)$O_{10}(OH)_8$, baileychlore (Rule and Radke, 1988)) and fraipontite ((Zn, Al)$_3$(Si, Al)$_2O_5(OH)_4$ (Cesàro, 1927)). Note that the thermodynamic calculations indicated a lower solubility of Zn in the presence of Zn-chlorite than in equilibrium with Zn-kerolite or Zn-LDH. Based on the average local coordination of Zn in Zn-chlorite (LDH-type and phyllosilicate-type layers in Zn-chlorite) and fraipontite (octahedral sheet with LDH-like composition and only one adjacent tetrahedral sheet), we assume that the EXAFS spectra of these species would resemble a mixture of Zn-kerolite and Zn-LDH. As a fifth possibility, small fractions of Zn-kerolite in LCF dominated by Zn-LDH might serve as a proxy for Zn inner-spherically adsorbed at the edges of clay minerals. The EXAFS of this type of Zn sorption complex is characterized by the cancellation of second shell contributions from light atoms in the octahedral sheet and nearest Si neighbors in the tetrahedral sheets and the presence of a signal from next-nearest Si neighbors (Schlegel et al., 2001; Schlegel and Manceau, 2006). The signal from next-nearest Si is also prominent in ZnMg-kerolite reference spectra (Schlegel et al., 2001). Thus, small fractions of ZnMg-kerolite fit in addition to a major fraction of Zn-LDH might partly account for Zn adsorbed at the edges of clay minerals.

4.4   *Formation of hydrozincite in soils*

In the soils SIS and TAL with highest Zn loadings, around half of the Zn was contained in hydrozincite (Table 8, Fig. 9). However, none of the μ-EXAFS spectra from the clayey matrix of soil SIS indicated any hydrozincite, even if collected close to the surface of calcareous particles. In contrast, pure hydrozincite crusts were observed on isolated limestone particles without direct contact with the clayey matrix (Table 7, Fig. 8). This observation is in agreement with a laboratory study showing that Al and Si in solution

promote Zn-phyllosilicate formation at the expense of hydrozincite precipitation (Tiller and Pickering, 1974) and with our thermodynamic calculations of Zn solubility in equilibrium with Zn-bearing phases, showing that Zn-kerolite and Zn-LDH are thermodynamically more stable than hydrozincite if Si and Al are present (Fig. 11). Microbially mediated precipitation of hydrozincite at nearly neutral pH has previously been documented in a stream contaminated by discharge from mine tailings (Podda et al., 2000). Based on a first-shell Zn-O distance obtained from EXAFS shell fitting, Hansel et al. (2001) postulated that hydrozincite had formed on the roots of wetland plants grown at a contaminated site. Furthermore, hydrozincite formation in calcareous soils has been postulated based on thermodynamic data (Schindler et al., 1969). However, this is the first study in which neoformed hydrozincite has been unequivocally identified in soil.

5   Conclusions

In contaminated calcareous soils, precipitation of Zn-phyllosilicate, Zn-LDH, and hydrozincite allows accumulation of increasing amounts of Zn exceeding the capacity for Zn uptake by adsorption, thereby limiting the leaching of Zn to deeper soil horizons and groundwater. The fraction of Zn in precipitates strongly depends on total Zn content and the availability of adsorption sites. Bulk and local Zn speciation inferred from EXAFS spectroscopy are in line with thermodynamic calculations on the solubility of Zn in the presence of various Zn-bearing phases and indicate that Zn-LDH and Zn-phyllosilicate are preferably formed over hydrozincite in the presence of Al and Si. Because these precipitates only form at increasing saturation of adsorption sites, their attenuating effect on the short-term bioavailability of Zn is likely limited. In addition, accumulated Zn precipitates are readily mobilizable in the presence of complexing agents or under

acidifying conditions. Thus, changes in soil chemical conditions might cause the release of previously accumulated Zn. This study focused on soils contaminated by aqueous Zn in the runoff water from galvanized power line towers. However, the same trends in Zn speciation are expected to apply to increasing amounts of Zn released from the weathering of Zn bearing contaminants or the decomposition of Zn-containing sewage sludge.

Acknowledgements

References

Adriano, D. C., 2001. *Trace Elements in Terrestrial Environments: Biogeochemistry, Bioavailability, and Risks of Metals.* Springer, New York.

Allada, R. K., Peltier, E., Navrotsky, A., Casey, W. H., Johnson, C. A., Berbeco, H. T., and Sparks, D. L., 2006. Calorimetric determination of the enthalpies of formation of hydrotalcite-like solids and their use in the geochemical modeling of metals in natural waters. *Clays Clay Miner.* 54, 409-417.

Allison, J. D., Brown, D. S., and Novo-Gradac, K. J., 1991. MINTEQA2/PRODEFA2, a geochemical assessment model for environmental systems. *U.S. Environemtal Protection Agency.*

Alloway, B. J., 1995. *Heavy Metals in Soils.* Chapman & Hall, London.

Bertling, S., Wallinder, I. O., Leygraf, C., and Kleja, D. B., 2006. Occurrence and fate of corrosion-induced zinc in runoff water from external structures. *Sci. Total Environ.* 367, 908-923.

Cesàro, G., 1927. Sur la fraipontite, silicate basique hydraté de zinc et d'alumine. *Anal. Soc. Geol. Be.* 50, B106-111.

Decarreau, A., 1980. Cristallogène expérimentale des smectites magnésiennes: hectorite, stévensite. *Bull. Mineral.* 103, 570-590.

Depège, C., El Metoui, F.-Z., Forano, C., De Roy, A., Dupuis, J., and Besse, J.-P., 1996. Polymerization of silicates in layered double hydroxides. *Chem. Mater.* 8, 952-960.

Elzinga, E. J. and Reeder, R. J., 2002. X-ray absorption spectroscopy study of Cu^{2+} and Zn^{2+} adsorption complexes at the calcite surface: Implications for site-specific metal

incorporation preferences during calcite crystal growth. *Geochim. Cosmochim. Acta* 66, 3943-3954.

Feng, X. H., Liu, F., Tan, W. E., and Liu, X. W., 2004. Synthesis of birnessite form the oxidation of Mn^{2+} by O_2 in alkali medium: effects of synthesis conditions. *Clay Miner.* 52, 240-250.

Ford, R. G. and Sparks, D. L., 2000. The nature of Zn precipitates formed in the presence of pyrophyllite. *Environ. Sci. Technol.* 34, 2479-2483.

Gee, G. and Or, D., 2002. Particle size analysis. In: Dane, J. H. and Topp, C. C. Eds., *Methods of Soil Analysis. Part4. Physical Methods*. Soil Science Society of America, Madison, USA.

Genin, P., Delahayevidal, A., Portemer, F., Tekaiaelhsissen, K., and Figlarz, M., 1991. Preparation and characterization of alpha-type nickel hydroxides obtained by chemical precipitation - study of the anionicspecies. *Eur. J. Solid State Inorg. Chem.* 28, 505-518.

Giovanoli, R., Stähli, E., and Feitknecht, W., 1970. Über Oxidhydroxide des vierwertigen Mangans mit Schichtengitter. *Helvetica Chimica Acta* 27, 209-220.

Gleyzes, C., Tellier, S., and Astruc, M., 2002. Fractionation studies of trace elements in contaminated soils and sediments: a review of sequential extraction procedures. *Trac-Trend Anal. Chem.* 21, 451-467.

Hansel, C. M., Fendorf, S., Sutton, S., and Newville, M., 2001. Characterization of Fe plaque and associated metals on the roots of mine-waste impacted aquatic plants. *Environ. Sci. Technol.* 35, 3863-3868.

Hendershot, W. H. and Duquette, M., 1986. A simple chloride method for determining cation exchange capacity and exchangeable cations. *Soil Sci. Soc. Am. J.* 50, 605-608.

Isaure, M.-P., Laboudigue, A., Manceau, A., Sarret, G., Tiffrau, C., Trocellier, P., Lamble, G. M., Hazemann, J. L., and Chateigner, D., 2002. Quantitative Zn speciation in a contaminated dredged sediment by μ-PIXE, μ-SXRF, EXAFS spectroscopy and principal component analysis. *Geochim. Cosmochim. Acta* 66, 1549-1567.

Isaure, M.-P., Manceau, A., Geoffroy, N., Laboudigue, A., Tamura, N., and Marcus, M. A., 2005. Zinc mobility and speciation in soil covered by contaminated dredged sediment using micrometer-scale and bulk-averaging X-ray fluorescence, absorption and diffraction techniques. *Geochim. Cosmochim. Acta* 69, 1173-1198.

Johnson, C. A. and Glasser, F. P., 2003. Hydrotalcite-like minerals ($M_2Al(OH)_6(CO_3)_{0.5}.XH_2O$, where M = Mg, Zn, Co, Ni) in the environment: synthesis, characterization and thermodynamic stability (vol 51, pg 1, 2003). *Clays Clay Miner.* 51, 357-357.

Juillot, F., Morin, G., Ildefonse, P., Trainor, T. P., Benedetti, M., Galoisy, L., Calas, G., and Brown, G. E., 2003. Occurrence of Zn/Al hydrotalcite in smelter-impacted soils from northern France: Evidence from EXAFS spectroscopy and chemical extractions. *Am. Mineral.* 88, 509-526.

Kheboian, C. and Bauer, C. F., 1987. Accuracy of selective extraction procedures for metal speciation in model aquatic sediments. *Anal. Chem.* 59, 1417-1423.

Kirpichtchikova, T. A., Manceau, A., Spadini, L., Panfili, F., Marcus, M. A., and Jacquet, T., 2006. Speciation and solubility of heavy metals in contaminated soil using X-ray

microfluorescence, EXAFS spectroscopy, chemical extraction, and thermodynamic modeling. *Geochim. Cosmochim. Acta* 70, 2163-2190.

Lanson, B., Drits, V. A., Gaillot, A.-C., Silvester, E., Plançon, A., and Manceau, A., 2002. Structure of heavy-metal sorbed birnessite: Part 1. Results from X-ray diffraction. *Am. Mineral.* 87, 1631-1645.

Lothenbach, B., Furrer, G., and Schulin, R., 1997. Immobilization of heavy metals by polynuclear aluminium and montmorillonite compounds. *Environ. Sci. Technol.* 31, 1452-1462.

Malinowski, E. R., 1977. Determination of the number of factors and the experimental error in a data matrix. *Anal. Chem.* 49.

Malinowski, E. R., 1978. Theory of error for target factor analysis with applications to mass spectrometry and nuclear magnetic resonance spectrometry. *Anal. Chim. Acta* 103, 339-354.

Manceau, A., Boisset, M. C., Sarret, G., Hazemann, R. L., Mench, M., Cambier, P., and Prost, R., 1996. Direct determination of lead speciation in contaminated soils by EXAFS spectroscopy. *Environ. Sci. Technol.* 30, 1540-1552.

Manceau, A., Lanson, B., Schlegel, M. L., Harge, J. C., Musso, M., Eybert-Berard, L., Hazemann, J. L., Chateigner, D., and Lamble, G. M., 2000. Quantitative Zn speciation in smelter-contaminated soils by EXAFS spectroscopy. *Am. J. Sci.* 300, 289-343.

Manceau, A., Marcus, M. A., and Tamura, N., 2002. Quantitative speciation of heavy metals in soils and sediments by synchrotron X-ray techniques. In: Fenter, P. A., Rivers, M. L., Sturchio, N. C., and Sutton, S. R. Eds., *Application of synchrotron*

radiation in low-temperature geochemistry and environmental science. Mineralogical Society of America, Washington, DC.

Manceau, A., Tamura, N., Celestre, R. S., MacDowell, A. A., Geoffroy, N., Sposito, G., and Padmore, H. A., 2003. Molecular-scale speciation of Zn and Ni in soil ferromanganese nodules from loess soils of the Mississippi Basin. *Environ. Sci. Technol.* 37, 75-80.

Manceau, A., Marcus, M. A., Tamura, N., Proux, O., Geoffroy, N., and Lanson, B., 2004. Natural speciation of Zn at the micrometer scale in a clayey soil using X-ray fluorescence, absorption, and diffraction. *Geochim. Cosmochim. Acta* 68, 2467-2483.

Manceau, A., Tommaseo, C., Rihs, S., Geoffroy, N., Chateigner, D., Schlegel, M. L., Tisserand, D., Marcus, M. A., Tamura, N., and Zueng-Sang, C., 2005. Natural speciation of Mn, Ni, and Zn at the micrometer scale in a clayey paddy soil using X-ray fluorescence, absorption, and diffraction. *Geochim. Cosmochim. Acta* 60, 4007-3034.

Marcus, M. A., MacDowell, A. A., Celestre, R. S., Manceau, A., Miler, T., Padmore, H. A., and Sublett, R. E., 2004. Beamline 10.3.2 at ALS: a hard X-ray microprobe for environmental and materials science. *J. Synchrotron Rad.* 11, 239-247.

Marcus, M. A., Manceau, A., and Kersten, M., 2004. Mn, Fe, Zn and As speciation in a fast-growing ferromanganese marine nodule. *Geochim. Cosmochim. Acta* 68, 3125-3136.

Merlino, S. and Orlandi, P., 2001. Carraraite and zaccagnaite, two new minerals from the Carrara marble quarries: their chemical compositions, physical properties, and structural features. *Am. Mineral.* 86, 1293-1301.

Nachtegaal, M., Marcus, M. A., Sonke, J. E., Vangronsveld, J., Livi, K. J. T., Van der Lelie, D., and Sparks, D. L., 2005. Effects of in situ remediation on the speciation and bioavailability of zinc in a smelter contaminated soil. *Geochim. Cosmochim. Acta* 69, 4649-4664.

Newville, M., 2001. IFEFFIT: interactive XAFS analysis and FEFF fitting. *J. Synchrotron Rad.* 8, 322-324.

Panfili, F. R., Manceau, A., Sarret, G., Spadini, L., Kirpichtchikova, T., Bert, V., Laboudigue, A., Marcus, M. A., Ahamdach, N., and Libert, M. F., 2005. The effect of phytostabilization on Zn speciation in a dredged contaminated sediment using scanning electron microscopy, X-ray fluorescence, EXAFS spectroscopy, and principal components analysis. *Geochim. Cosmochim. Acta* 69, 2265-2284.

Podda, F., Zuddas, P., Minacci, A., Pepi, M., and Baldi, F., 2000. Heavy metal coprecipitation with hydrozincite [$Zn_5(CO_3)_2(OH)_6$] from mine waters caused by photosynthetic microorganisms. *Appl. Environ. Microbiol.* 66, 5092-5098.

Preis, W. and Gamsjager, H., 2001. (Solid plus solute) phase equilibria in aqueous solution. XIII. Thermodynamic properties of hydrozincite and predominance diagrams for ($Zn^{2+}+H_2O+CO_2$). *J. Chem. Thermodyn.* 33, 803-819.

Ravel, B. and Newville, M., 2005. Athena, Artemis, Hephaestus: data analysis for X-ray absorption spectroscopy using IFEFFIT. *J. Synchrotron Rad.* 12, 537-541.

Reeder, R. J., Lamble, G. M., and Northrup, P. A., 1999. XAFS study of the coordination and local relaxation around Co^{2+}, Zn^{2+}, Pb^{2+}, and Ba^{2+} trace elements. *Am. Mineral.* 84, 1049-1060.

Rodrigues-Filho, U. P., Vaz Jr., S., Felicissimo, M. P., Scarpellini, M., Cardoso, D. R., Vinhas, R. C. J., Landrers, R., Schneider, J. F., McGarvey, B. R., Andersen, M. L.,

and Skibsted, L. H., 2005. Heterometallic manganese/zinc-phytate complex as model compound for metal storage in wheat grains. *J. Inorg. Biochem.* 99, 1973-1982.

Rule, A. C. and Radke, F., 1988. Baileychlore, the Zn end member of the trioctahedral chlorite series. *Am. Mineral.* 73, 135-139.

Saeed, M. and Fox, R. L., 1977. Relations between suspension pH and zinc solubility in acid and calcareous soils. *Soil Sci.* 124, 199-204.

Sarret, G., Balesdent, J., Bouziri, L., Garnier, J. M., Marcus, M. A., Geoffroy, N., Panfili, F., and Manceau, A., 2004. Zn speciation in the organic horizon of a contaminated soil by micro-x-ray fluorescence, micro- and powder-EXAFS spectroscopy, and isotopic dilution. *Environ. Sci. Technol.* 38, 2792-2801.

Scheinost, A. C., Kretzschmar, R., Pfister, S., and Roberts, D. R., 2002. Combining selective sequential extractions, X-ray absorption spectroscopy, and principal component analysis for quantitative zinc speciation in soil. *Environ. Sci. Technol.* 36, 5021-5028.

Schindler, P., Reinert, M., and Gamsjäger, H., 1969. Löslichkeitskonstanten und freie Bildungsenthlapien von $ZnCO_3$ und $Zn_5(OH)_6(CO_3)_2$ bei 25°C. *Helvetica Chimica Acta* 52, 2327-2332.

Schlegel, M. L., Manceau, A., Charlet, L., and Hazemann, J. L., 2001. Adsorption mechanisms of Zn on hectorite as a function of time, pH, and ionic strength. *Am. J. Sci.* 301, 798-830.

Schlegel, M. L. and Manceau, A., 2006. Evidence for the nucleation and epitaxial growth of Zn phyllosilicate on montmorillonite. *Geochim. Cosmochim. Acta* 70, 901-917.

Schosseler, P. M., Wehrli, B., and Schweiger, A., 1999. Uptake of Cu^{2+} by the calcium carbonates vaterite and calcite as studied by continuous wave (CW) and pulse electron paramagnetic resonance. *Geochim. Cosmochim. Acta* 63, 1955-1967.

Schuwirth, N., Voegelin, A., Kretzschmar, R., and Hofmann, T., 2007. Vertical distribution and speciation of trace metals in weathering flotation residues of a zinc/lead sulfide mine. *J. Environ. Qual.* 36, 61-69.

Shan, X. Q. and Bin, C., 1993. Evaluation of sequential extraction for speciation of trace-metals in model soil containing natural minerals and humic acid. *Anal. Chem.* 65, 802-807.

Sharpless, R. G., Wallihan, E. F., and Peterson, F. F., 1969. Retention of zinc by some arid zone soil materials treated with zinc sulfate. *Soil Sci. Soc. Am. P.* 33, 901-904.

Taylor, R. M., 1984. The rapid formation of crystalline double hydroxy salts and other compounds by controlled hydrolysis. *Clay Miner.* 19, 591-603.

Tiller, K. G. and Pickering, J. G., 1974. Synthesis of zinc silicates at 20°C and atmospheric pressure. *Clays Clay Miner.* 22, 409-416.

VBBo, 1998. Verordnung über Belastungen des Bodens (Swiss Ordinance relating to Impacts on Soil). *SR 814.12, Eidgenössische Drucksachen und Materialzentrale, Bern, Switzerland.*

Vieillard, P., 2002. New method for the prediction of Gibbs free energies of formation of phyllosilicates (10 Å and 14 Å) based on the electronegativity scale. *Clays Clay Miner.* 50, 352-363.

Voegelin, A. and Kretzschmar, R., 2005. Formation and dissolution of single and mixed Zn and Ni precipitates in soil: Evidence from column experiments and extended X-ray absorption fine structure spectroscopy. *Environ. Sci. Technol.* 39, 5311-5318.

Voegelin, A., Pfister, S., Scheinost, A. C., Marcus, M. A., and Kretzschmar, R., 2005. Changes in zinc speciation in field soil after contamination with zinc oxide. *Environ. Sci. Technol.* 39, 6616-6623.

Voegelin, A., Tokpa, G., Jacquat, O., Barmettler, K., and Kretzschmar, R., 2008. Zinc fractionation in contaminated soils by sequential and single extractions: Influence of soil properties and zinc content. *J. Environ. Qual.* 37, 1190-1200.

Waychunas, G. A., Fuller, C. C., and Davis, J. A., 2002. Surface complexation and precipitate geometry for aqueous Zn(II) sorption on ferrihydrite: I. X-ray absorption extended fine structure spectroscopy analysis. *Geochim. Cosmochim. Acta* 66, 1119-1137.

Webb, S. M., 2005. SIXPack: a graphical user interface for XAS analysis using IFEFFIT. *Phys. Scr.* T115, 1011-1014.

Zeien, H. and Brümmer, G. W., 1989. Chemische Extraktionen zur Bestimmung von Schwermetallbindungsformen in Böden. *Mitt. Dtsch. Bodenkundl. Ges.* 59, 505-510.

TABLES

2   **Table 1:** Physical and chemical properties and Zn content of the studied soil materials.

Soil	Geology	pH (CaCl$_2$)	TOC (g/kg)	TIC (g/kg)	Texture (g/kg) Clay	Silt	Sand	ECEC[a] (mmol$_c$/kg)	Tower age[b] (years)	Total Zn (mg/kg)	Zn/clay[c] (mg/kg)	Exch. Zn[d] (mg/kg)
GLO	Limestone	6.6	49	1.2	451	319	230	406	30	1322	2900	194
LUC2	Dolomite	7.3	33	87	88	131	781	181	55	1398	15900	12
BAS	Limestone	6.4	74	4.4	382	434	184	263	30	12170	31900	2548
LAUS	Limestone	6.2	44	6.5	406	348	246	164	39	13810	34000	2838
TAL	Limestone	7.5	14	89	108	244	648	99	39	6055	56100	20
SIS	Limestone	6.5	59	17	309	288	403	371	39	30090	97400	3'052

3   [a]effective cation exchange capacity. [b]indicating duration of soil contamination. [c]total Zn content divided by clay content (i.e., concentration in clay
4   fraction if clay fraction contained all Zn). [d]exchangeable Zn in 0.1 M BaCl$_2$ at solution-soil-ratio of 30 mL/g.

1   **Table 2.** Results of the principal component analysis of 12 bulk- and 23 μ-EXAFS spectra.

Component	Eigenvalue	Variance	Cum. Var.[a]	IND[b]
1	179.4	0.441	0.441	0.01042
2	60.6	0.149	0.591	0.00567
3	16.6	0.040	0.632	0.00541
4	12.9	0.031	0.663	0.00535
5	11.4	0.028	0.691	0.00532
6	9.9	0.024	0.716	0.00537
7	8.7	0.021	0.737	0.00547
8	8.0	0.019	0.757	0.00560

2   [a]Cumulative variance. [b]Indicator function (Malinowski, 1977).

1   **Table 3.** Target testing of reference spectra using the first five components obtained by

2   PCA (Table 2).

References	SPOIL[a]	NSSR (%)
aqueous Zn	1.2	4.0
hydrozincite	1.5	4.4
Zn-kerolite	1.6	2.5
$Zn_{0.8}Mg_{0.2}$-kerolite	1.9	2.1
$Zn(OH)_2$	2.0	8.3
Zn-phytate	2.4	4.4
Zn-LDH	2.5	1.7
$Zn_{0.6}Mg_{0.4}$-kerolite	2.6	2.7
low Zn-birnessite	2.7	13.9
Zn sorbed calcite	2.8	3.6
$Zn_{0.34}Mg_{0.66}$-kerolite	2.8	7.5
smithsonite	2.9	32.9
Zn sorbed ferrihydrite	3.0	4.4
$Zn_{0.06}Mg_{0.94}$-kerolite	3.2	12.8
Zn-phosphate	3.2	6.0
Zn-calcite	3.7	34.9
high Zn-birnessite	4.4	29.4
Zn-HIM	6.3	41.7
Zn-lithiophorite	10.3	38.1

3   [a]SPOIL classification (Malinowski, 1978): 0-1.5
4   excellent; 1.5-3 good; 3-4.5 fair; 4.5-6 acceptable;
5   >6 unacceptable reference.

1   **Table 4:** Linear combination fits of the μ-EXAFS from thin-section of the soil GLO (Fig.3).

Spectrum	Zn-LDH	sorbed $^{IV}Zn^a$	aqueous Zn	low Zn-birnessite	Sum	NSSR
	(%)	(%)	(%)	(%)	(%)	(%)
GLO-1	93	———	17	———	110	3.9
GLO-2	———	90 (Ph)	22	———	112	4.0
GLO-3	———	39 (Fh)	54	———	93	9.9
GLO-4	———	99 (Fh)	———	———	99	8.7
GLO-5	———	65 (Fh)	———	37	102	12.2

2   [a](Ph): Zn-phytate, (Fh): Zn sorbed ferrihydrite.

1 **Table 5:** Linear combination fits of μ-EXAFS spectra from the thin-sections of the soil LUC2 (Fig. 5).

Spectrum	hydrozincite	Zn-LDH	Zn-kerolite[a]	sorbed ^{IV}Zn[b]	aqueous Zn	Sum	NSSR
	(%)	(%)	(%)	(%)	(%)	(%)	(%)
LUC2-1	———	———	———	84 (Ph)	23	107	5.5
LUC2-2	———	32	———	54 (Cc)	15	101	4.9
LUC2-3	———	———	22 (80Zn)	36 (Cc)	51	109	4.2
LUC2-4 Fit A	———	———	93 (80Zn)	———	———	93	3.5
LUC2-4 Fit B	———	126	———	———	———	126	10.4
LUC2-5	40	32	35 (60Zn)	———	———	107	2.6
LUC2-6	51	36	———	———	21	108	4.8
LUC2-7	———	60	———	36 (Cc)	13	109	3.8
LUC2-8 Fit A	———	———	87 (80Zn)	———	———	87	10.5
LUC2-8 Fit B	———	127	———	———	———	127	3.3
LUC2-8 Fit C	———	103	18 (80Zn)	———	———	121	2.8
LUC2-9	———	103	19 (80Zn)	———	———	122	1.9

2 [a](80Zn): $Zn_{0.8}Mg_{0.2}$-kerolite, (60Zn): $Zn_{0.6}Mg_{0.4}$-kerolite, [b](Ph): Zn-phytate, (Cc): Zn sorbed calcite.

1 **Table 6:** Linear combination fits of the μ-EXAFS spectra from the thin-section of the soil SIS (Fig.7).

Spectrum	Zn-LDH	$Zn_{0.8}Mg_{0.2}$-kerolite	sorbed $^{IV}Zn^a$	aqueous Zn	Sum	NSSR
	(%)	(%)	(%)	(%)	(%)	(%)
SIS-1	37	———	61 (Cc)	———	98	5.0
SIS-2	———	———	73 (Cc)	31	104	3.9
SIS-3	———	———	76 (Cc)	26	102	6.2
SIS-4	75	19	25 (Cc)	———	119	2.2
SIS-5	79	15	27 (Fh)	———	121	2.5
SIS-6	118	———	———	———	118	9.8
SIS-7	67	13	39 (Cc)	———	119	2.2
SIS-8	78	17	22 (Cc)	———	117	1.7
SIS-9	56	36	23 (Cc)	———	112	1.9

2 ^{a}(Cc): Zn sorbed calcite, (Fh): Zn sorbed ferrihydrite.

1 **Table 7:** Linear combination fits of Zn K-edge EXAFS spectra from limestone particles and crusts and limestone particles (Fig. 8).

Spectrum[a]	hydrozincite	Zn-LDH	Zn-kerolite[b]	sorbed ^{IV}Zn[c]	Zn-calcite	Sum	NSSR
	(%)	(%)	(%)	(%)	(%)	(%)	(%)
GLO-WP	———	30	———	62 (Cc)	13	105	9.5
LUC2-WP	47	———	20 (80Zn)	27 (Cc)	———	94	2.8
TAL-WP	78	———	19 (60Zn)	———	———	97	2.9
SIS-WPC	85	———	———	———	———	85	0.4
LAUS-RPC	38	———	27 (60Zn)	36 (Fh)	———	101	2.2
SIS-RPC	33	———	47 (80Zn)	25 (Fh)	———	105	3.8

2 [a]WP=white limestone particles, WPC=white limestone particle crust, RPC=red limestone particle crust. [b](80Zn): $Zn_{0.8}Mg_{0.2}$-
3 kerolite, (60Zn): $Zn_{0.6}Mg_{0.4}$-kerolite, [c](Cc): Zn sorbed calcite, (Fh): Zn sorbed ferrihydrite.

1 **Table 8:** Linear combination fits of the EXAFS spectra of the bulk soil samples (Fig. 9).

Spectrum	hydrozincite	Zn-LDH	Zn-kerolite[a]	sorbed ^{IV}Zn[b]	aqueous Zn	Sum	NSSR	Σppt[c]	Σsorbed[d]
	(%)	(%)	(%)	(%)	(%)	(%)	(%)	(%)	(%)
GLO	———	20	———	50 (Fh)	31	101	5.0	20	81
LUC2	———	———	29 (80Zn)	56 (Fh)	21	106	4.9	29	77
BAS	———	40	13 (80Zn)	26 (Cc)	22	101	0.8	53	48
LAUS	———	36	13 (80Zn)	34 (Cc)	17	100	1.3	49	51
TAL	52	———	25 (80Zn)	24 (Cc)	———	101	3.6	77	24
SIS	51	30	———	———	16	97	1.1	81	16

2 [a](80Zn): $Zn_{0.8}Mg_{0.2}$-kerolite, (60Zn): $Zn_{0.6}Mg_{0.4}$-kerolite, [b](Cc): Zn sorbed calcite, (Fh): Zn sorbed ferrihydrite, [c]sum of
3 precipitate species (hydrozincite, Zn-LDH, and Zn-kerolite), [d]sum of sorbed species (sorbed ^{IV}Zn and aqueous Zn).

Figure captions

Fig. 1. Zn K-edge EXAFS spectra of selected Zn references (solid lines) and target transforms (dots) calculated with the first five components obtained from principal component analysis (Tables 2 and 3).

Fig. 2. Light microscope images of the GLO soil thin section and corresponding μ-XRF maps (black: lowest intensity; white: 90% of highest recorded intensity in map). (A) Coarse map of a 3000×1150 μm^2 area (20×20 μm^2 resolution, 100 ms dwell time). (B) and (C) Fine maps of 470×500 μm^2 area (5×5 μm^2 resolution, 100 ms dwell time).

Fig. 3. μ-EXAFS spectra from the GLO soil thin section (solid lines) and LCF spectra (dots). LCF results are provided in Table 4.

Fig. 4. Light microscope images of the LUC2 soil thin section and corresponding μ-XRF maps for Zn, Ca, Fe and Mn (black: lowest intensity; white: 90% of highest recorded intensity in map). (A) Coarse map of a 3000×2000 μm^2 area (20×20 μm^2 resolution, 100 ms dwell time). (B) Fine map of a 200×150 μm^2 area and (C) fine map of a 700×500 μm^2 area (5×5 μm^2 resolution, 100 ms dwell time).

Fig. 5. μ-EXAFS spectra from thin sections of soil LUC2 (solid lines) and LCF spectra (dots). LCF results are provided in Table 5.

Fig. 6. Light microscope images of the SIS soil thin section and corresponding μ-XRF maps (black: lowest intensity; white: 90% of highest recorded intensity in map). (A) Coarse map of a 3600×2400 μm^2 area (20×20 μm^2 resolution, 200 ms dwell time). (B) Fine map of a 360×240 μm^2 area (5×5 μm^2 resolution, 150 ms dwell time).
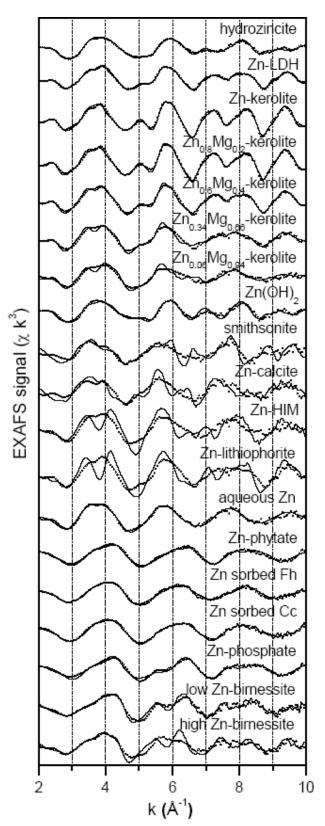
Fig. 7. μ-EXAFS spectra collected on the SIS soil thin section (solid lines) and LCF spectra (dots). LCF results are provided in Table 6.
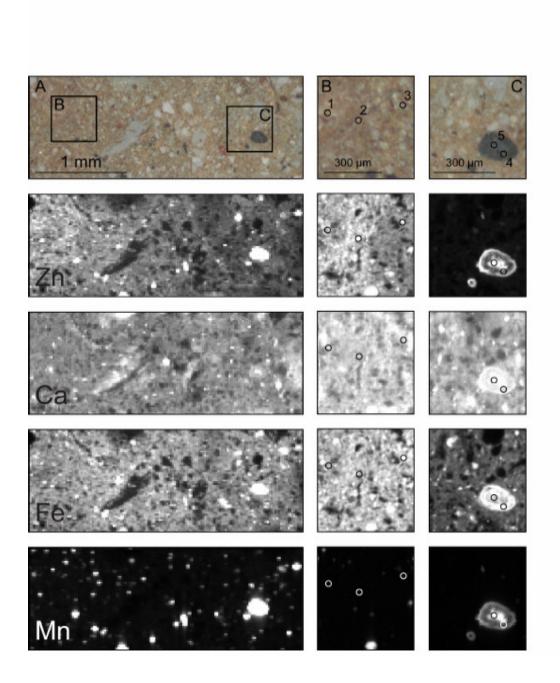
Fig. 8. EXAFS spectra collected from white limestone particles (WP), white limestone particle crusts (WPC) and red limestone particle crusts (RPC) (solid lines) and LCF spectra (dots). LCF results are provided in Table 7.

Fig. 9. EXAFS spectra of the bulk soil samples (solid lines) and LCF spectra (open dots). LCF results are provided in Table 8.

Fig. 10. Fractionation of Zn by sequential extraction. Results for uncontaminated soil and quartz powder spiked with Zn-kerolite, Zn-LDH, and hydrozincite and for contaminated soil samples.

Fig. 11. Solubility of Zn^{2+} in equilibrium with selected Zn-bearing phases. "low CO_2" and "high CO_2" denote calculations at atmospheric (3.2×10^{-4} atm) and hundredfold atmospheric CO_2 partial pressure. "low Al" and "high Al" denote calculations with Al^{3+} in equilibrium with gibbsite and amorphous $Al(OH)_3$, respectively. "low Si" and "high Si" calculations consider silicic acid in equilibrium with quartz ("low Si") and amorphous SiO_2 ("high Si").
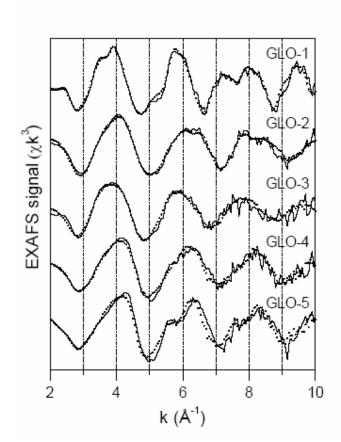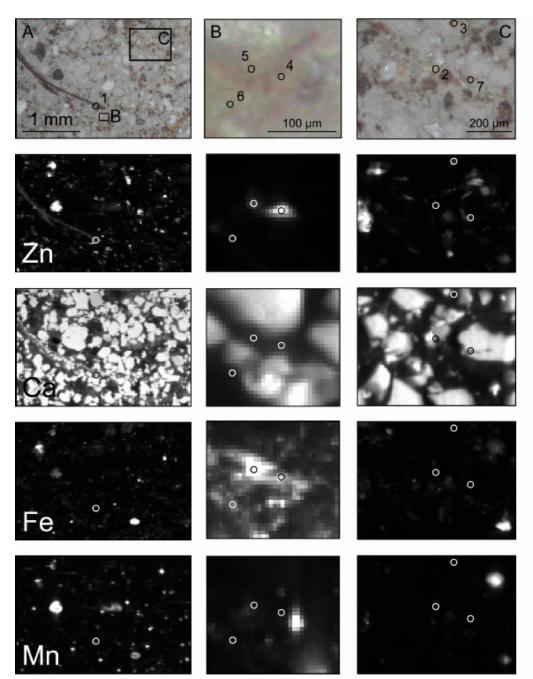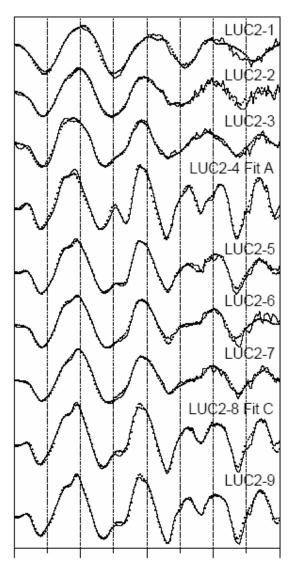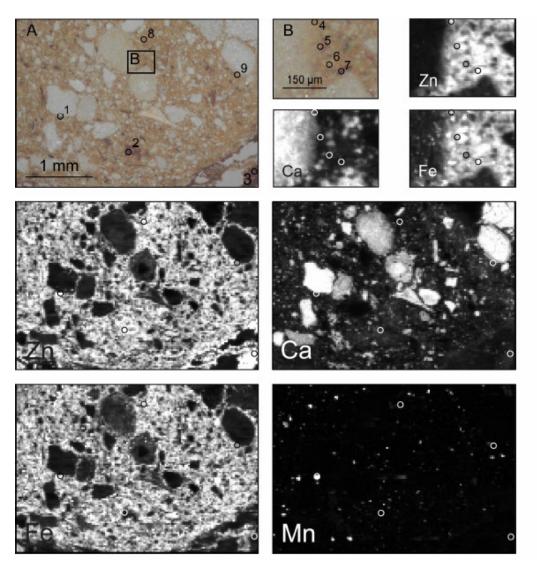
Fig.1

Fig.2

Fig.3

Fig.4

Fig.5

LUC2-1
LUC2-2
LUC2-3
LUC2-4 Fit A
LUC2-5
LUC2-6
LUC2-7
LUC2-8 Fit C
LUC2-9

Fig.6

Fig.7

Fig.8

Fig.9

Fig.10

Fig.10

F7 XRF-values
F6 0.1 *M* ascorbic acid + F5, pH 3.25
F5 0.2 *M* NH$_4$-oxalate, pH 3.25
F4 0.025 *M* NH$_4$-EDTA, pH 4.6
F3 0.1 *M* NH$_2$OH-HCl + F2, pH 6.0
F2 1 *M* NH$_4$-acetate, pH 6.0
F1 1 *M* NH$_4$NO$_3$

Fig.11

am. Zn(OH)$_2$
ZnO
ZnCO$_3$, low CO$_2$
ZnCO$_3$, high CO$_2$
hydrozincite, low CO$_2$
hydrozincite, high CO$_2$
Zn-LDH, low CO$_2$ & Al
Zn-LDH, high CO$_2$ & Al
Zn-kerolite, low Si
Zn-kerolite, high Si
Zn-chlorite, low Si & Al
Zn-chlorite, high Si & Al